

TRL-5 EMCCD Controller for Space Applications

Olivier Daigle^a, Jérémy Turcotte^a, Oleg Djazovski^b, Éric Gloutnay^b, Frédéric Grandmont^c,
James Veilleux^c, Deven Patel^d, Simon Thibault^d

^aNüvü Camēras, 603-355 Peel, Montréal, QC, H3C 2G9, Canada

^bCanadian Space Agency, 6767 route de l'Aéroport, St-Hubert, QC, J3Y 8Y9, Canada

^cABB Inc., 3400 Pierre-Ardouin Quebec, QC, G1P 0B2, Canada

^dCOPL, Université Laval, 2325 Rue de l'Université, Quebec, QC, G1V 0A6, Canada

Abstract. We present the progress in characterization of a Nüvü Camēras CCD Controller for Counting Photons (CCCP) designed for extreme low light imaging in space environment with the 1024×1024 Teledyne-e2V EMCCD detector (the CCD201-20). The EMCCD controller was designed using space qualified parts before being extensively tested in thermal vacuum. The performance test results include the readout noise, clock-induced charges, dark current, dynamic range and EM gain. We also discuss the CCCP's integration in the coronagraph of the High-Contrast Imaging Balloon System project: a fine-pointing and optical payload for a future Canadian stratospheric balloon mission. This first space qualified EMCCD controller, named CCCPs, will enhance sensitivity of the future low-light imaging instruments for space applications such as the detection, characterization and imaging of exoplanets, search and monitoring of asteroids and space debris, UV imaging, and satellite tracking.

Keywords: EMCCD, Space Qualified Electronics, Faint Flux Imaging, Clock Induced Charges, Dark Current, High Contrast Imaging, Space Debris, Exoplanets.

1 INTRODUCTION

Since Electron Multiplying CCD (EMCCD) became commercially available in early 2000, ground-based applications of those devices have flourished: adaptive optics, hyperspectral imaging, high resolution spectroscopy, time-resolved photometry, etc. Although several recent studies were made on the impact of the space environment¹⁻³ on the EMCCD devices for flight applications, very little was published on the optimization of the electronic controller. This paper presents the EMCCD controller developed by Nüvü Camēras for demanding applications of an astronomical space mission, which is based on the same core technology as its commercial EMCCD controllers. This technology has demonstrated its ability to yield low Clock Induced Charges (CIC) as the same time as a low dark current on the CCD60, CCD97, and CCD201-20 from Teledyne-e2v^{4,5} and, more recently, on the 4k × 4k CCD282.⁶ This paper presents the characterization results of the EMCCD space controller in the context of extreme low light imaging for space applications.

2 SYSTEM OVERVIEW

The system was designed to clock an EMCCD at a nominal read-out frequency of 10 MHz through its Electron Multiplying (EM) amplifier, as well as to allow the read-out of the EMCCD through its Conventional (CONV) amplifier at low speed and low noise. This allows an EMCCD to operate also as a Charge Coupled Device (CCD), which broadens the incoming light flux range in which the device will reach its maximum efficiency. However, the greatest challenge involved was achieving the same level of CIC with the newly developed system as the one that is achieved with

Table 1 Performance requirements of the EMCCD sensor as adopted by the Canadian Space Agency.

Ref.	Parameter	Requirement
0.0	Array format	1024 × 1024 pixels
0.1	Clock Induced Charges	< 0.001ē/s
0.2	Bandpass	400-1100 nm
0.3	Dark current	< 0.001ē/s
0.4	Camera controller EM gain	> 3000
0.5	Dynamic range	> 42 dB

Nüvü Camēras’ commercial cameras. This achievement is required to reach the highest low flux performance.

As the system design inputs we have used the performance goals for the Wide-Field Infrared Survey Telescope (WFIRST) mission from the Table 3.8 of the Science Definition Team (SDT) 2015 document.⁷ Those criteria and goals are summarized in Tabled 1 and 2, respectively.

Performance Evaluation Criteria (PEC) 0.2 and performance goals 1.x are met by the use of a CCD201-20 with midband antireflection coating.⁸ PEC 0.0 and performance goals 2.x are met by the use of a CCD201-20 without the coating.⁸ The other PEC and performance goals 3.x were dependent on both the EMCCD device used and the controlling electronics. They were checked for compliance.

In order to meet those requirements, the system was designed to provide the following:

- Generation of 14 Low Voltage analog clocks with a refresh rate 160 MHz (6.25 ns) and 14 bits of resolution with a ±15 volts span;
- Generation of 1 High Voltage clock (up to 50 Volts) with a frequency of 10 MHz, a 1 ns timing resolution and an adjustable low and high level with 8 and 12 bits of resolution respectively;
- Digitization of two video outputs (non simultaneously) to accommodate both the EM and Conventional outputs of the CCD201-20. The digitization is be possible at 14 bits, 10 MHz with analog CDS and at 14 bits, 40 MHz with a digital CDS implemented in VHSIC Hardware Description Language (VHDL);
- 10 DC levels with the possibility to adjust them (8 bits);
- A Camera Link (CL) interface for communication of the pixel data to a host and an input for commands.

The goal of the project was to demonstrate that the camera sensitivity was not negatively impacted by the new design of the low and high voltage clocks, the video digitization chains, and the bias generation whilst developing a read-out electronics that was as close as possible to a flight electronics, at a fraction of the cost. Hence, throughout the project, the design aimed to be as close as possible to one that could technically fly even if some aspects of space qualification

Table 2 WFIRST performance goals for the single photon counting camera.

Ref.	Parameter	Goal	Comments
1.0	QE at 660nm	88%	From [7], matched to CCD201-20 ⁸
1.1	QE at 770nm	68%	From [7], matched to CCD201-20 ⁸
1.2	QE at 890nm	28%	From [7], matched to CCD201-20 ⁸
2.0	Active area	1024 × 1024	Matched to CCD201-20 ⁸
2.1	Pixel pitch	13 μ m	Matched to CCD201-20 ⁸
2.2	Device architecture	Frame transfer	Matched to CCD201-20 ⁸
2.3	PRNU	TBD	Matched to CCD201-20 ⁸
2.4	Fill factor	100%	Matched to CCD201-20 ⁸
2.5	Bad pixels		CCD201-20 grade 1 specification ⁸
2.6	Bad columns		CCD201-20 grade 1 specification ⁸
3.0	Active area FW	>20k \bar{e}	Optimized for low light imaging
3.1	EM register FW	>200k \bar{e}	Optimized for low light imaging
3.2	Dark current @ $\geq -110^{\circ}\text{C}$	$\leq 0.0001\bar{e}/\text{pix}/\text{s}$	From [7], $> -110^{\circ}\text{C}$ for good CTE, IMO
3.3	CIC	$\leq 0.0018\bar{e}/\text{pix}/\text{im}$	From [7], @ gain of 1000, IMO
3.4	Read-out noise	80 \bar{e}	At 10 MHz, @ gain of 1
3.5	Non-linearity	$\pm 1\%$	100kHz, Conv output, 90% of pixel FW
3.6	Non-linearity	$\pm 1\%$	10 MHz, @ gain 1, 90% of pixel FW
3.7	Non-linearity	$\pm 3\%$	10 MHz, @ gain 1000, 50% of EM FW

would not be tested. The system was designed and built with Space Qualified (SQ) or engineering models Integrated Circuits (ICs), or their exact commercial equivalent. The parts were chosen so that the SQ version would sustain the radiation at the environment of L2 orbit for several years. Since the ICs of the controller are either radiation tolerant or radiation hardened by design and it was assembled with a few commercial equivalent parts to save costs, the radiation tolerance was not tested at board-level. The routing of the Printed Circuit Board (PCB) was made with dual footprints to accommodate the SQ and engineering models ICs. Although, the controller did not undergo vibration testing. Best practices usually employed for optimizing the hardware for space applications were employed for the PCB design: the routing was made according to Class 3 of the IPC-2221/2222 standard for the highest level of reproducibility; the board was designed to have a thickness of 93 mils and has several mounting holes to better sustain vibrations; the material of the PCB was chosen to have a low outgassing. The radiation-tolerant Field-programmable Gate Array (FPGA) of the system was not programmed with radiation-aware code. The design phase allocated enough resources required to implement triple redundant logic, watchdogs, etc, but those were not implemented for the tests.

Since the strict requirements of the target mission (WFIRST), such as power, mass, and volume budgets, orbit, launch vehicle, etc have not been finalized, broad assumptions had to be made and several areas of the design could be revisited to better fit a particular mission.

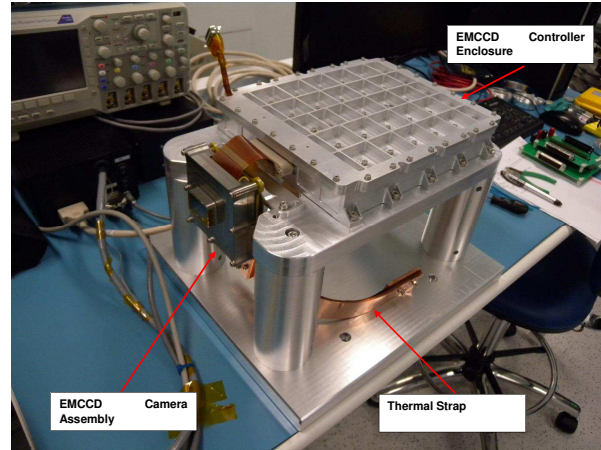
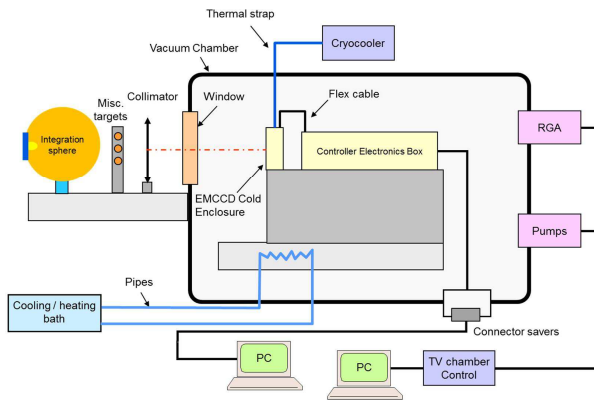


Fig 1 Tests set-up in ABB’s TVAC. **Left:** Schematics of the TVAC set-up. **Right:** Controller assembly with the CCD201-20 on its thermal stand.

3 TESTS DESCRIPTION

The camera was integrated with a CCD201-20. Two read-out modes were developed to read the EMCCD:

- 10 MHz of horizontal, and 1 MHz of vertical frequencies through the EM amplifier;
- 1 MHz of horizontal, and 1 MHz of vertical frequencies through the CONV amplifier.

Both of those read-out modes allow for the use of multiple Regions of Interest (ROIs).

The tests were performed at ABB’s facilities in Quebec City in a Thermal Vacuum Chamber (TVAC) that was pumped to $\sim 5 \cdot 10^{-7}$ Torr (Figure 1). The temperature of the electronics was regulated by a Julabo Cooling bath, and the EMCCD was cooled with a Cryomech cryocooler. The temperature of the EMCCD was then read-out with a PT100 Resistance Temperature Detector (RTD) and regulated with a 10 W heater to $\pm 0.01^\circ\text{C}$ at the sensing point.

The following tests were performed while maintaining the electronics at 20°C and the EMCCD at -85°C :

- Characterize the EMCCD and associated controller Read-out Noise (RON) and k-gain at the fastest pixel rate achievable by the controller;
- Measure the system’s linearity deviation and Vertical Full Well through the EM amplifier;
- Characterize the EMCCD and associated controller RON and k-gain at a slow pixel read-out through the conventional amplifier;
- Measure the system’s linearity deviation and Vertical Full Well through the CONV amplifier;

Those tests allowed to check the compliance of the system with the PEC 0.5, and performance goals 3.0, 3.4, 3.5, and 3.6.

Next, the temperature of the EMCCD was varied from -75°C to -105°C whilst the electronics were kept at 20°C . The tests performed were the following:

- Characterize the EMCCD gain at the fastest pixel rate achievable by the controller;
- Characterize the CIC generated by the read-out process of the EMCCD gain at the fastest pixel rate achievable by the controller;
- Characterize the dark current generated by the EMCCD as a function of its temperature.

Those tests allowed to check the compliance of the system with the PEC 0.1, 0.3, 0.4, goals 3.1, 3.2, 3.3, and 3.7.

Then, the temperature of the EMCCD was kept at -85°C , and the temperature of the electronics were varied from -10°C to 40°C . The following tests were the performed:

- Characterize the EMCCD and associated controller RON and k-gain at the fastest pixel rate achievable by the controller;
- Characterize the EMCCD gain at the fastest pixel rate achievable by the controller.

Finally, the system was exposed to a temperature of 65°C while unpowered to test for its survival.

4 TESTS RESULTS

4.1 RON, Linearity, and VFW Measurements Through the EM Amplifier at 10 MHz at Unity Gain

The RON and Vertical Full Well (VFW) are measured by using the Photon Transfer Curve (PTC) method by illuminating EMCCD with a stable light source (LED) while increasing the exposure time to vary the amount of accumulated photons. The method yields at the same time the reciprocal gain of the system (k-gain) and the linearity can be inferred since the change in the exposure time yields a linearly increasing signal. The RON and k-gain are related to the horizontal shifting and are therefore independent from the VFW if one assumes that the horizontal shifting capacity ($\bar{\epsilon}$) will always be greater than the vertical shifting capacity. In the case of the CCD201-20, this is true for unity EM gain since the vertical and horizontal charge handling capacity are $<80\text{ k}\bar{\epsilon}$, and $>200\text{ k}\bar{\epsilon}$, respectively.⁸

The PTC of the TRL-5 system at 10 MHz through the EM amplifier is shown in Figure 2. The data shows that the system's response is $35.1\text{ }\bar{\epsilon}/\text{ADU}$, and the read-out noise is $174\bar{\epsilon}$, which means that the standard deviation of a bias image is 4.95 ADU . The acquisition was made with a vertical clocking frequency of 1 MHz, up to a pixel well of $\sim 35\text{ k}\bar{\epsilon}$ with a linearity within the $\pm 1\%$ range. The linearity at low flux ($<10\sigma$) is always a challenge to measure, which explains the scattering of the data points for fluxes $<1\text{ k}\bar{\epsilon}$.

By taking into account the $35\text{ k}\bar{\epsilon}$ of VFW and the RON of $174\bar{\epsilon}$, the dynamic range is of 46 dB with vertical clocks of 1 MHz.

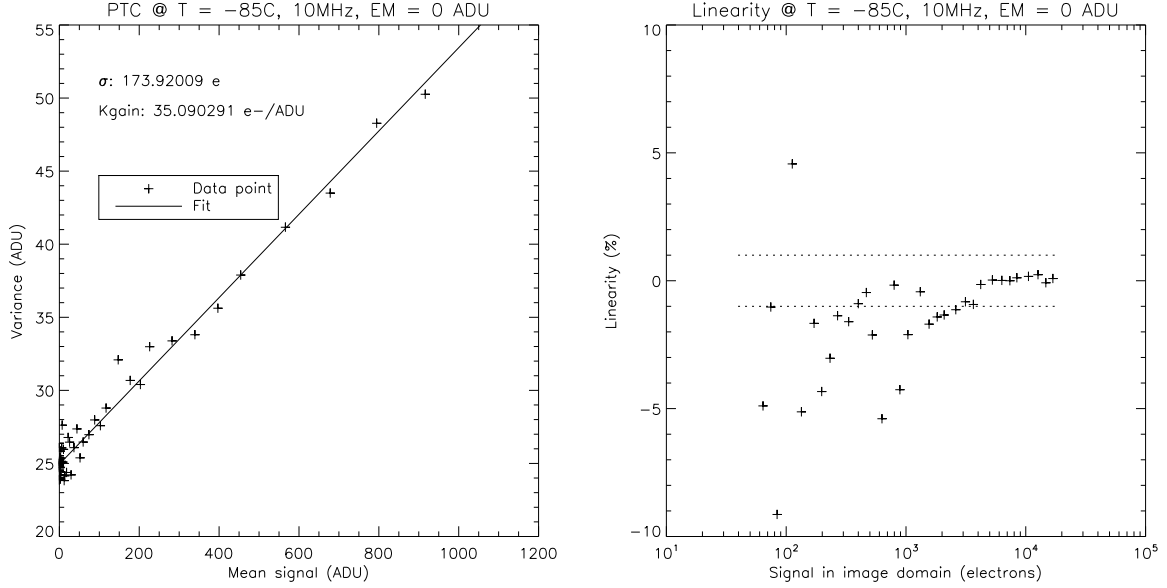


Fig 2 PTC results for EM at 10 MHz. **Left:** Photon Transfer Curve. **Right:** Linearity. The dotted line shows the $\pm 1\%$ boundaries.

4.2 EM Gain Characterization Through the EM Amplifier at 10 MHz

At temperatures of -75C, -85C, -95C, and -105C, the EM gain and effective RON were measured for logarithmically increasing High Voltage (HV) clock amplitudes. The effective RON as a function of the EM gain was measured through the EM gain characterization process. Since the Excess Noise Factor (ENF) artificially lowers the measured reciprocal gain of the system (k-gain, \bar{e}/ADU), it has to be taken into account when measuring the effective RON at non-unity EM gain. The measurement of the ENF is made through this process. The theoretical values for the ENF were derived by [9] and are expected to follow the equation

$$ENF = \sqrt{2(M-1)M^{-\frac{N+1}{N}} + \frac{1}{M}},$$

where M is the mean EM gain and N is the number of multiplication elements in the EM register.

For all temperatures of the EMCCD, the EM gain was calibrated at up to 5000. Figure 3 shows the relation between the command of the HV clock amplitude (controlled by a 12 bits low speed Digital to Analog Converter (DAC)) and the measured EM gain as a function of the temperature of the EMCCD.

The results of effective RON results of shown in Figure 4. The minimum achieved effective RON is $<0.05 \bar{e}$. The data shows a slight increase of the effective RON with respect to the theoretical value for EM gains >500 . This behaviour is explained by a coupling between the HV clock and the output signal of the EMCCD. A phantom HV clock, that can be explained by substrate bouncing, is observed in the video signal, which creates a correlation between the measured RON

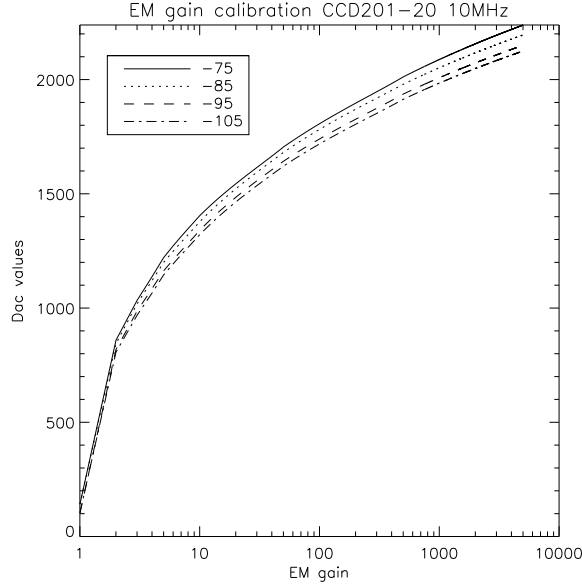


Fig 3 EM Gain Calibration Results for EMCCD Temperature Between -75 and -105°C.

and the EM gain. As the HV clock amplitude is increased to yield a higher EM gain, the substrate bouncing becomes higher and so does its effect on the measured RON.

The linearity at an EM gain of 1000 is also measured during the EM gain characterization process. At -85°C, the EM gain of 1000 is achieved for a DAC value of 2059 Analog to Digital Unit (ADU). Figure 5 shows the linearity measured with the PTC data. The linearity curve is almost fully constrained within the $\pm 3\%$ boundaries up to a full well of $\sim 400 \text{ k}\bar{e}$ ($400 \bar{e}$ in the image domain with an EM gain of 1000). This also shows that the EM register Full Well (FW) is $>400 \text{ k}\bar{e}$.

The right panel of Figure 5 shows the measurement of the ENF. Even though the data points are not perfectly aligned with the theoretical curve, the discrepancies should not be associated to an ENF that varies from the predicted value. This simply outlines the fact that the ENF measurement method used does not yield an extremely high Signal to Noise Ratio (SNR). However, the trend of the measured ENF allows one to trust that the EMCCD behaves as predicted by the theory.

4.3 Dark Current and CIC Measurements

In order to separate the horizontal and vertical CIC components, the EMCCD is over-scanned in both the vertical and horizontal directions (see Figure 6).

The "Image" represents the active portion of the detector that is collecting the light. The data for total background signal measurement is taken from this region. The data represents the total unwanted signal that would appear in an image (dark current and CIC). The "Overscan" is the portion of the detector that undergoes only a horizontal transfer. Hence, the horizontal CIC is measured in this region. Finally, the "OverscanV" consists of the sum of the horizontal and vertical

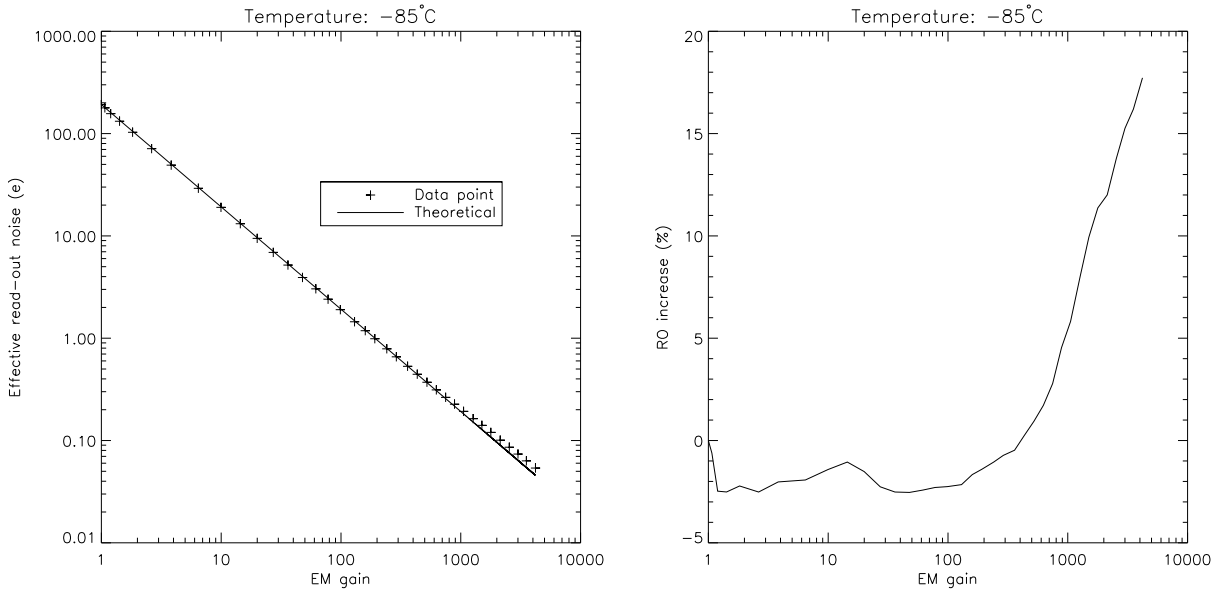


Fig 4 Effective RON Measurements. **Left:** Effective RON as a Function of the Measured EM gain, Where the Theoretical Curve is $\sigma_{G=0}/G$. **Right:** Effective Noise Excess as Compared to $\sigma_{G=0}/G$.

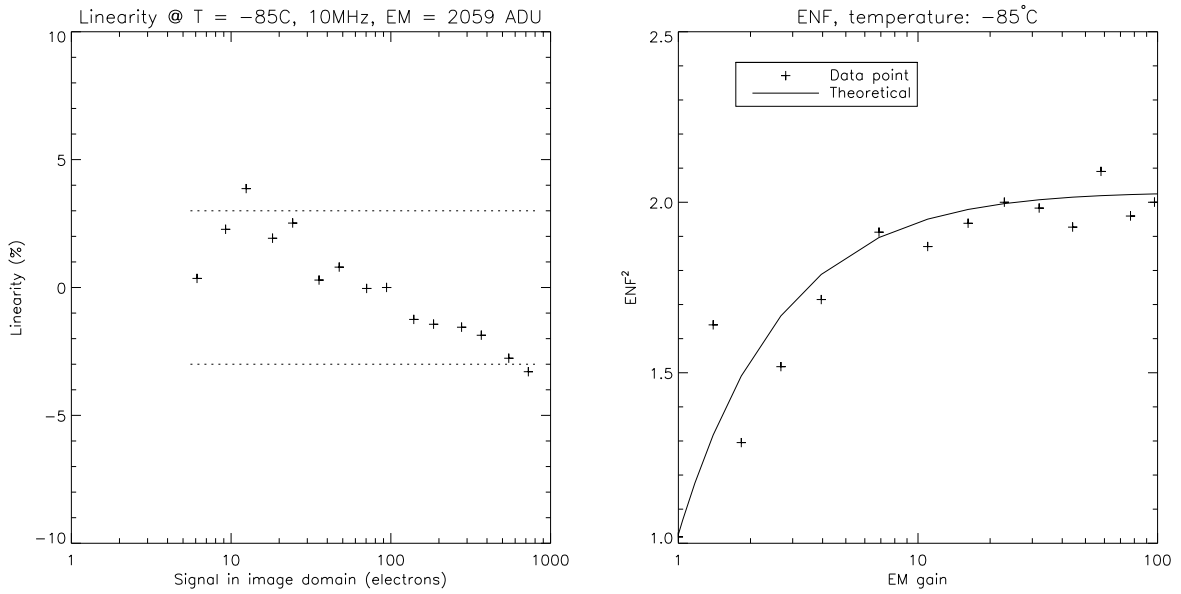


Fig 5 Left: Linearity Measurement at an EM Gain of 1000. The Dotted line shows the $\pm 3\%$ boundaries. **Right:** Measured and theoretical ENF.

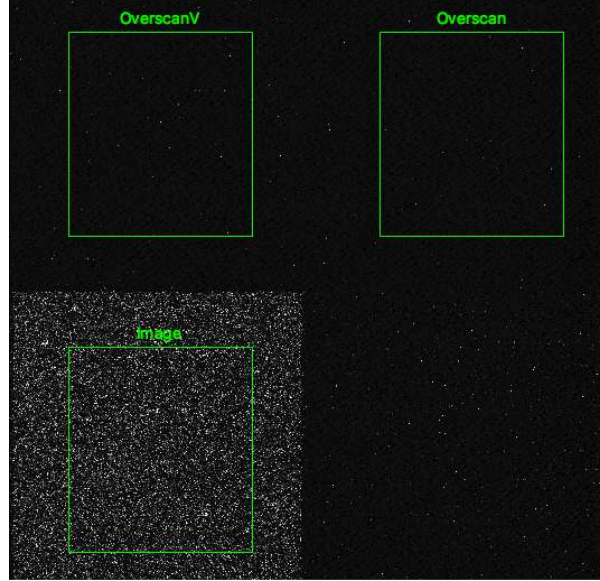


Fig 6 Overscan scheme used for the dark current and CIC measurements.

CIC. Hence, the vertical CIC is taken as the signal level of this region minus the signal of the "Overscan" region.

The total background signal was measured with a 0s effective exposure time. Thus, the total background signal measurement includes the dark current generated during the read-out process as well as the CIC. The measurement errors are within $0.0002 \bar{e}/\text{pixel}/\text{im}$ which explains the discrepancy between the total background signal measured and the sum of the horizontal and vertical CIC. The vertical frequency used is 1 MHz, which yields the lowest vertical CIC level. The measurements are made with a 5σ threshold to reflect the Photon Counting operation.

The dark current measurements are performed at an EM gain of 1000. The dark current is measured by fitting a slope to the signal acquired by the camera for exposures from 0 to 64 seconds.

The CIC results are presented in Tables 3 to 6. The dark current results are presented in Table 7. Figure 7 shows an example of the data acquired to measure both the background signal, the horizontal and vertical CIC, as well as the dark current.

The horizontal CIC is roughly independent of the temperature, as it stays around $0.0008 \bar{e}/\text{pix}/\text{im}$ regardless of the temperature, within the measurement errors. The measured vertical CIC does seem to vary with temperature, but it is the impact of the dark current generated during the read-out process. Hence, the colder the temperature, the less charges are generated during the read-out. Even though both the horizontal and vertical CIC seem to increase with the EM gain, it is partly the result of the increased photon counting efficiency due to the higher G/σ ratio.¹⁰

4.4 RON, Linearity, and VFW Measurements Through the CONV Amplifier at 100 kHz

Those measurements were performed with the same method as described in Section 4.1. The Analog to Digital Converter (ADC) of the controller, is not capable of sampling in Correlated Double Sampling (CDS) at 100 kHz (it is limited to 5 MHz). As a result, in order to read-out the

Table 3 Background signal and CIC at -75C.

EM gain	Bkgd ($\bar{e}/\text{pix/im}$)	H CIC ($\bar{e}/\text{pix/im}$)	V CIC ($\bar{e}/\text{pix/im}$)
1000	0.00153	0.00093	0.00077
2000	0.00339	0.00218	0.00157
3000	0.00480	0.00313	0.00205
5000	0.00685	0.00466	0.00267

Table 4 Background signal and CIC at -85C.

EM gain	Bkgd ($\bar{e}/\text{pix/im}$)	H CIC ($\bar{e}/\text{pix/im}$)	V CIC ($\bar{e}/\text{pix/im}$)
1000	0.00117	0.00075	0.00066
2000	0.00251	0.00163	0.00132
3000	0.00346	0.00236	0.00167
5000	0.00504	0.00375	0.00216

Table 5 Background signal and CIC at -95C.

EM gain	Bkgd ($\bar{e}/\text{pix/im}$)	H CIC ($\bar{e}/\text{pix/im}$)	V CIC ($\bar{e}/\text{pix/im}$)
1000	0.00084	0.00061	0.00028
2000	0.00165	0.00135	0.00053
3000	0.00270	0.00207	0.00081
5000	0.00396	0.00314	0.00106

Table 6 Background signal and CIC at -105C.

EM gain	Bkgd ($\bar{e}/\text{pix/im}$)	H CIC ($\bar{e}/\text{pix/im}$)	V CIC ($\bar{e}/\text{pix/im}$)
1000	0.00087	0.00071	0.00022
2000	0.00191	0.00153	0.00043
3000	0.00271	0.00202	0.00055
5000	0.00424	0.00357	0.00079

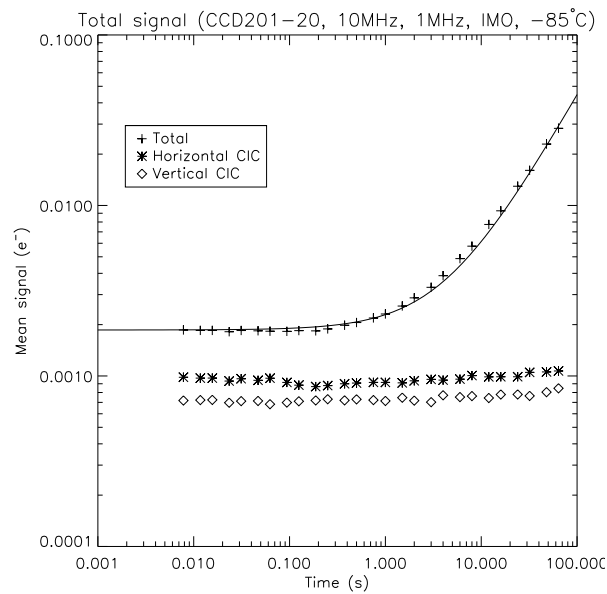


Fig 7 Total Background Signal Measured in PC at -85°C and at an EM Gain of 1000. The values are corrected for the events loss due to the PC threshold.

Table 7 Dark Current Measurements at 10 MHz

Temperature	Dark current ($\bar{e}/\text{pix/s}$)
-75C	0.002088
-85C	0.000651
-95C	0.000082
-105C	0.000053

EMCCD at 100 kHz of pixel rate, the digital CDS had to be implemented on the controller. This implies to drive the ADC in Sample & Hold (SAH) rather than using its internal CDS, and process the CDS digitally in the FPGA. For that purpose, the ADC is driven at its maximum frequency (40 MHz), which means that a total of 400 samples are acquired for every pixel. The digital CDS is given a table of weights that it applies to the pixel's samples to properly process the reference, signal, and unwanted samples. Slower read-out would even be possible since the ADC is not the limiting factor. Since the digital CDS can be given up to 2048 weights, it could read-out a CCD or EMCCD as slowly as ~ 20 kHz.

An additional benefit of the digital CDS is that it is capable of numerically increasing the signal's resolution. Even though the ADC is 14 bits, the results of the processing over 400 samples is well beyond the 16 bits resolution. As the theoretical increase in Effective Number of Bits (ENOB) is $\sqrt{n/4}$, where n is the number of samples *used* by the digital CDS, assuming an equal weight for all samples. This feature was not used.

The PTC of the TRL-5 system at 100 kHz through the CONV amplifier is show in Figure 8. The data shows that the system's response is $10.24\bar{e}/\text{ADU}$, and the read-out noise is $9.2\bar{e}$, which means that the standard deviation of a bias image is 0.9 ADU. The acquisition was made with a vertical clocking frequency of 1 MHz, up to a pixel well of $\sim 10\text{ k}\bar{e}$ with a linearity within the $\pm 1\%$ range.

The VFW was also measured with a vertical frequency of 500 kHz, which yields $\sim 77\text{ k}\bar{e}$ (Figure 9, with data acquired at 1 MHz pixel rate through the CONV amplifier).

4.5 Temperature Tests

The temperature tests were divided into two parts. The survival test was made in part by baking the controller to 65°C for 36 hours during the integration to outgas it. Then, it was run at temperatures set points of the cooling bath between -10°C and 40°C in 10°C increments and characterization data at every step. This has the advantage of measuring whether the controller's response drifts as a function of the temperature.

Hence, a PTC was run at every temperature step increment to measure the response of the EM output when running at 10 MHz. The tests were performed with the core of the controller at -4°C , 13°C , and 23°C . At 33°C , the controller could not be operated since the FPGA was not perfectly thermally coupled to the housing. Therefore, temperatures warmer than 33°C were not used. Even though the core of the problem was identified, time constraints prevented to put the controller back in the TVAC for another test run.

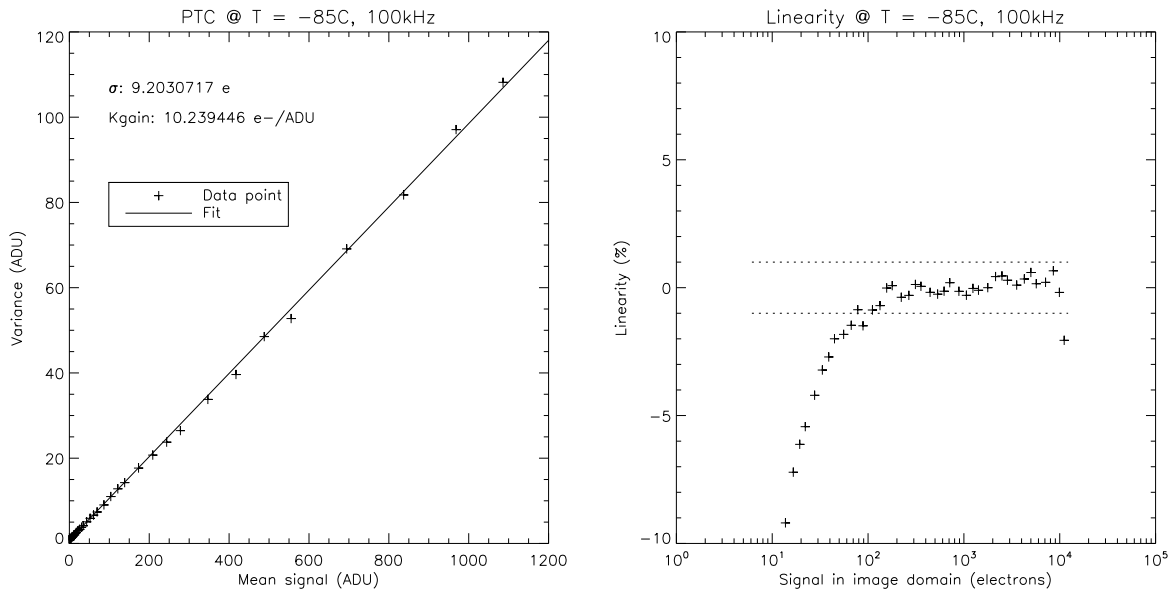


Fig 8 PTC Results for CONV at 100 kHz. **Left:** Photon Transfer Curve. **Right:** Linearity. The dotted line shows the $\pm 1\%$ boundaries.

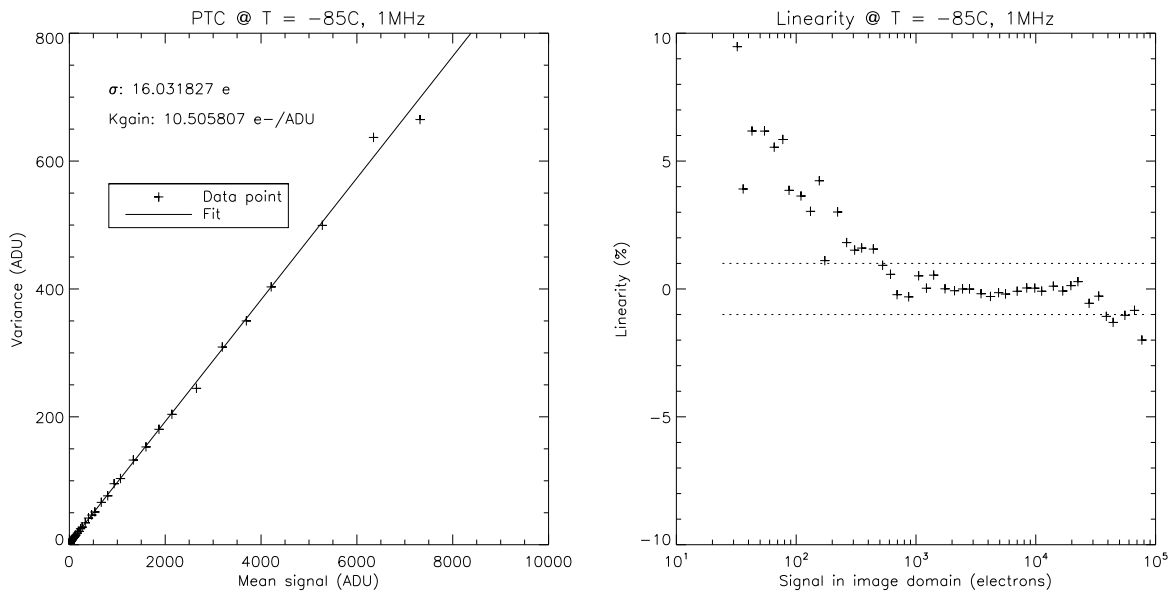


Fig 9 PTC Results for CONV at 1 MHz, 500 kHz Vertical Frequency. **Left:** Photon Transfer Curve. **Right:** Linearity. The dotted line shows the $\pm 1\%$ boundaries.

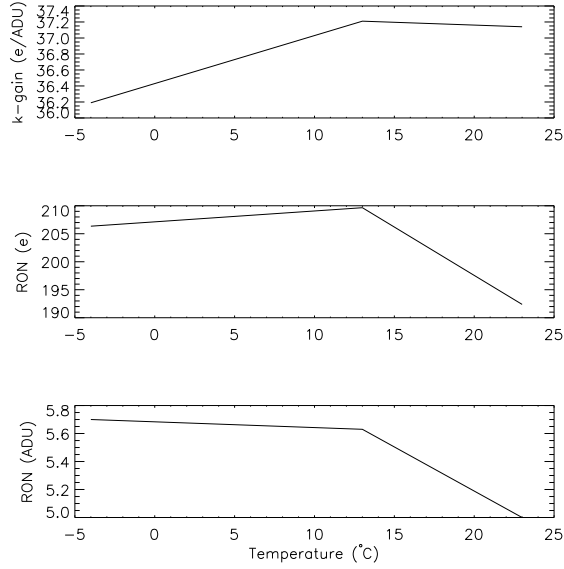


Fig 10 Stability of the PTC as a Function of the Controller’s Temperature. The results are shown for the k-gain (**top**), Read-out Noise in \bar{e} (**center**), and Read-out Noise in ADU (**bottom**).

The PTC results as a function of the controller’s temperature are presented in Figure 10. The results show a pretty good stability of the k-gain as a function of the temperature. As a matter of fact, they are within 3%, which could be accounted for the measurement errors. The RON (in \bar{e}) itself does not follow the same trend, and this can be explained by looking at the RON in ADU. There is a tendency of getting a lesser variance in the digital output of the images at the temperature of the controller increases, while the response does not change (k-gain). Hence, the video chains do not seem to exhibit a change in gain, which would affect the k-gain, but they rather exhibit a lesser noise. The exact reason for this behaviour is not yet identified.

5 DISCUSSIONS OF THE TESTS RESULTS

The CIC rate measured with the SQ controller was very similar to that achieved with Nüvü Camēras’ commercial controller. At an EM gain of 1000, the measurements were within the $0.001\bar{e}/\text{pix}/\text{im}$ range for temperatures $\leq -85^\circ\text{C}$. At warmer temperatures, the CIC measurements were contaminated by the dark current that is generated during the read-out, which is measured in the total background signal.

The minimum dark current achieved at -105°C was $0.000053\bar{e}/\text{pix}/\text{s}$, which is significantly lower than the requirement of $0.001\bar{e}/\text{pix}/\text{s}$. At -85°C , the dark current measured was $0.000651\bar{e}/\text{pix}/\text{s}$. It is important to note that the dark current can vary by almost an order of magnitude between devices. Hence, a few devices would have to be tested if a strict specification of dark current would arise for a mission.

The EM gain was characterized up to 5000, which is beyond the 3000 PEC. The controller would be capable of even higher EM gain since its HV clock is capable of a higher amplitude.

This gives room for a re-characterization of the EMCCD if an ageing would be measured. In this case, a higher HV clock is required to yield the same EM gain. It is important for the controller to have this capability to ensure that the EMCCD will make it possible to reach very low effective read-out noise through the full extent of a mission.

The dynamic range at 10 MHz and unity EM gain was measured to be 46 dB. A lower RON would benefit the dynamic range. The read-out with a vertical frequency of 500 kHz also improved the dynamic range since the VFW was increased from ~ 35 kē to ~ 77 kē. The impact of the slower vertical clocks would be to yield a higher level of CIC during the vertical transfer. This was however not measured through this study.

With respect to the WFIRST coronagraph imager's performance goals, the active area FW and EM register FW were measured and found to meet the goals. The clocking schemes used to fulfill these goals also yield the required CIC level. The linearity of the system was measured to be within the acceptable range, in both EM and CONV modes. The RON of the EM output, at unity EM gain, was found to be higher than the goal. In this case, the 14-bit ADC of the controller, as compared to the 16-bit ADC of Nüvü Camēras' commercial controller (that led to the 80-ē goal), makes it harder to yield a low read-out noise as well as a wide dynamic range (>400 kē in this case). In order to achieve the wide dynamic range while not saturating the ADC, a low response (or high k-gain) has to be implemented. This puts a higher stress on the digitization of the signal since even a low variance of the digitization will yield a high RON. It would be possible to alter the gain of the video chain of the EM output to circumvent this fact and reach a lower RON, at the cost of a lower EM register FW. The same logic applies to the CONV output since it is very difficult to get a RON in ADU that is significantly below 1 ADU. Hence, the high k-gain of the CONV output, required to match the ~ 100 kē VFW and allow vertical or horizontal binning, limits the RON one can achieve. In this case, it would be possible to benefit from the increased ENOB made possible by the digital CDS.

6 STRATOSPHERIC FLIGHT

An opportunity arose to fly the SQ system with a 512×512 CCD (CCD97) from Teledyne-e2v in a balloon to image at 40 km of altitude, in the HiCiBaS project^{11,12,a}. The main goal of this mission is to test a Low Order Wavefront Sensor (LOWFS) technology for balloon-based exoplanet imaging to compensate for inadequate pointing accuracy as well as to gather data about the atmospheric dynamics that are prevalent at the balloon altitude, which are mandatory for precision astronomy. This application has been identified as a pathfinder to future potential mission employing high contrast imaging. The schematic diagram of the HiCiBaS payload is presented in Figure 11. This concept outlines a complete system that would be required to image exoplanets with the help of a coronagraph.

While the primary objective of the project remains the study and characterization of the LOWFS performance at 40 km and the typical PSF instabilities and anomalies encountered at these altitudes

^a<http://hicibas.copl.ulaval.ca/index.html>

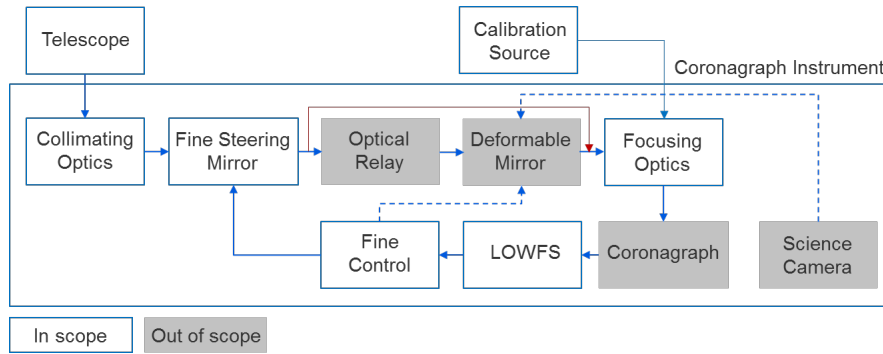


Fig 11 The HiCIBaS payload concept.

in the visible, this testbed allows further expansion into a more complete high contrast imaging observatory to be flown for dedicated exoplanet candidate observations. Follow-on activities that were suggested in the original project included:

1. Addition of a coronagraph and high sensitivity EMCCD camera.
2. Addition of a Deformable Mirror to further refine star flux rejection and WFEs control.
3. Replacement of the telescope for a larger unobscured aperture system (ex. 70 cm TMA similar to PILOT).
4. Addition of an Integral Field Spectrograph to perform spectroscopic observation of exoplanet candidates.

In the full mission concept, there are two cameras. The first one is a fast camera that is embedded in the LOWFS block (see also Figure 12), which in this case is a HNü 128 that Nüvü Camēras provides to the project. The second camera is the "science camera" that would be used to image the output of the coronagraph.

6.1 The coronagraph arm

The original HiCIBaS mission involves testing only the LOWFS. Hence, the coronagraph parts are out of scope. However, the evolution of this mission has raised interests among the scientific community to fly not only the LOWFS, but the coronagraph system as well. The following contributions have become available from collaborators: the Deformable Mirror (DM) is provided by Iris-AO, the coronagraph¹³ is provided by the Leiden University (Netherlands), the Real-Time Computer (RTC) is provided by the NASA, and Nüvü Camēras proposed to provide the science camera using the SQ controller that was developed.

Subsequently, the optical design of the HiCiBaS mission was thus modified to include the coronagraph arm (Figure 13) with the added components. On this figure, the "EMCCD 128" camera is the camera for the LOWFS, while the "EMCCD 512" camera is the science camera for the coronagraph arm. An example of the image at the focal plane of the science camera is shown in

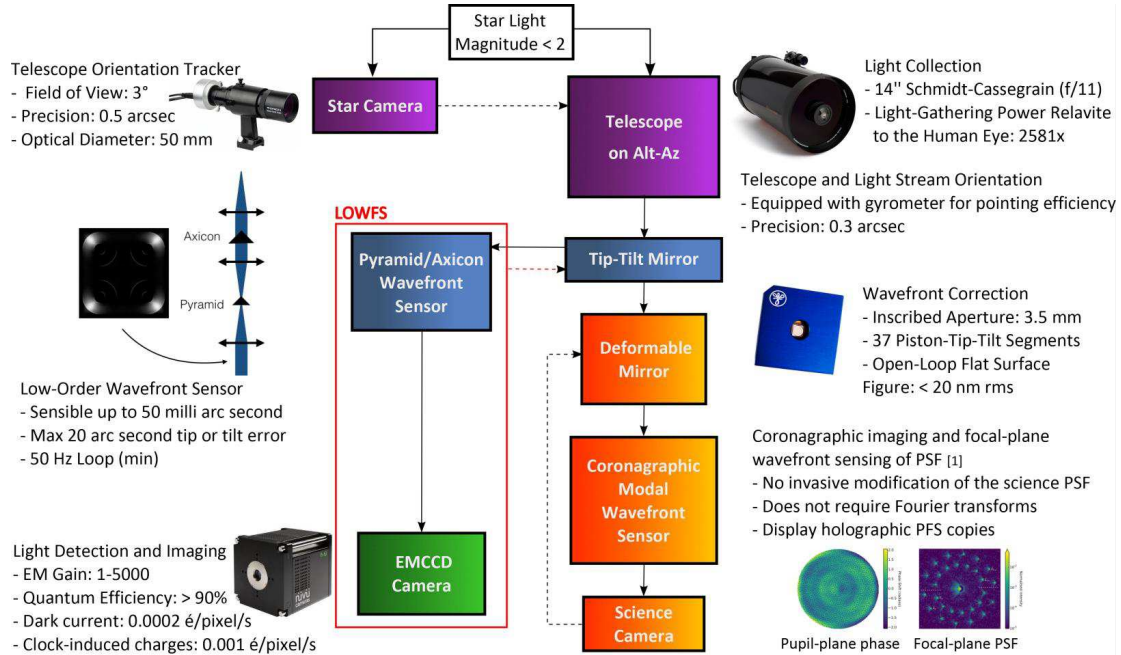


Fig 12 The HiCIBaS schematic of the complete mission concept.

Figure 14. The crowding of the spatial structures that has to be imaged explains the relatively high spatial resolution that is required for this mission. Moreover, the space constraints on the balloon platform limits the length of the coronagraph bench to ~ 500 mm, which have an impact on its complexity with respect to the required spatial resolution and pixel pixel. The target wavelength for the observation is 850 nm.

6.2 Imaging requirements and EMCCD detector choice

The imaging requirements for the camera of the coronagraph arm of the HiCIBaS mission are outlined in Table 8. The requirements were compared to what can be achieved with the three mostly used scientific EMCCD detectors: the CCD60 (128×128), the CCD97 (512×512), and the CCD201-20 (1024×1024). The key performance parameters are discussed below:

- The spatial resolution requirement is matched to [13]. This allows for both the CCD97 and the CD201-20 to meet it;
- The temporal resolution is matched to [13]. With a read-out at 10 MHz of pixel rate, which is the limit of the TRL-5 system, this allows for both the CCD60 and the CCD97 to meet it, assuming that the read-out is $H \times 250$ pixels, where H is the width of the device (128, 512, and 1024 pixels respectively). It is important to mention that the horizontal cropping of the read-out area does not speed-up the read-out of the device as the full length of a line has to be read-out to flush the light that has fallen outside of the region of interest;

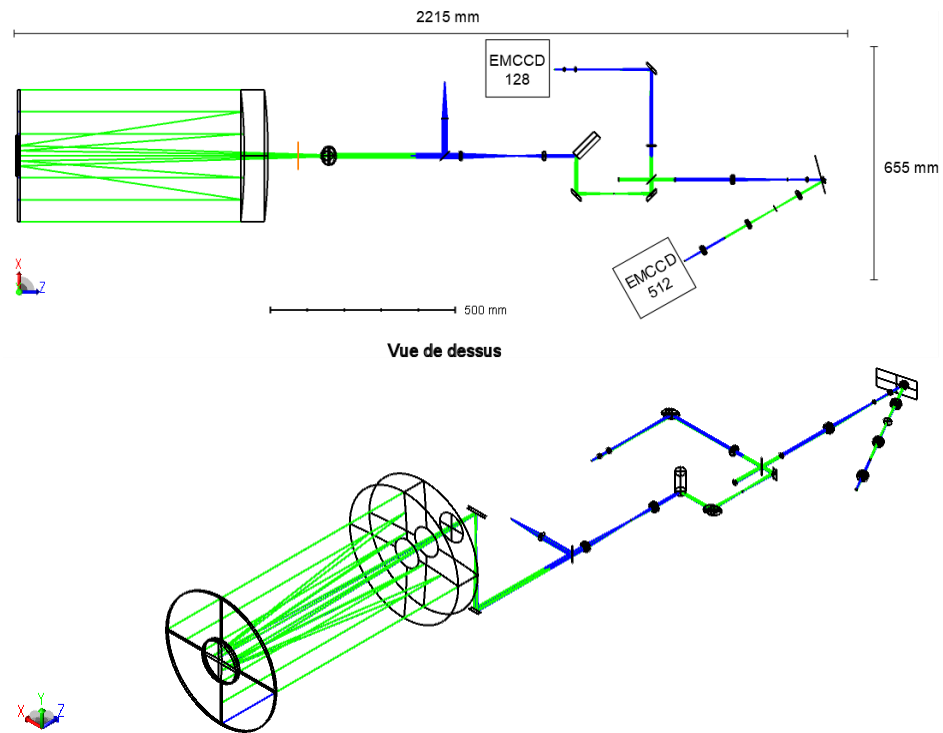


Fig 13 The complete HiCIBaS optical bench.

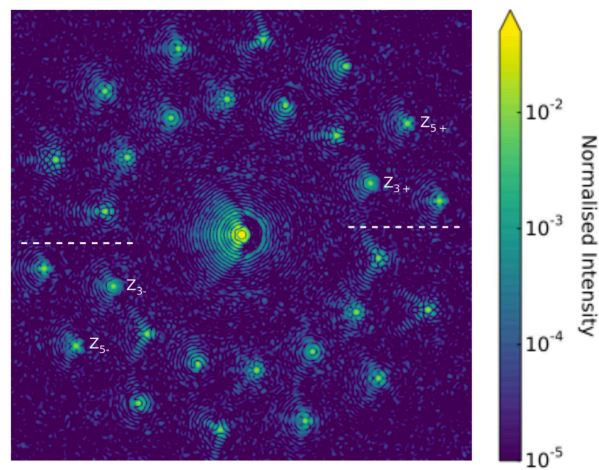


Fig 14 Example of the image at the focal place of the science camera (taken from [13]) to measure the various Zernike coefficients.

Table 8 Science camera requirements for the coronagraph arm of the HiCIBaS mission.

Parameter	Requirement	Performance of EMCCDs		
		CCD60	CCD97	CCD201-20
Spatial resolution	$\geq 250 \times 250$ pix	Worse	Best	Best
Temporal resolution	≤ 20 ms	Best	Best	Worse
Optical bench length/complexity	< 500 mm	Worse	Good	Best
Spectral bandwidth	850 nm	Good	Best	Best

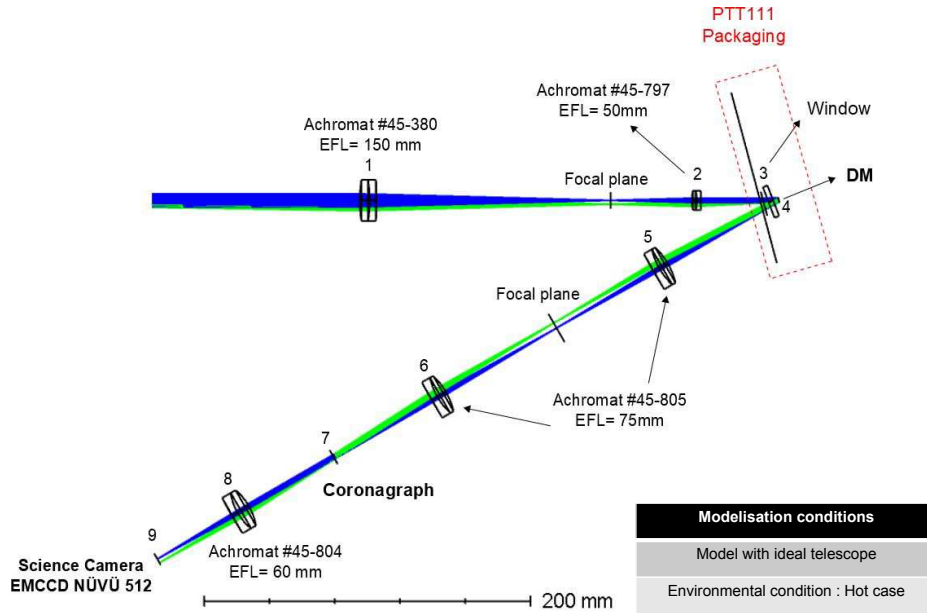


Fig 15 The HiCIBaS coronagraph optical bench.

- The optical bench length and complexity is explained by the necessity to illuminate a patch to 250×250 pixels on the detector. Hence, the smaller the pixels the lower the magnification. A higher magnification would imply either a longer optical bench or faster optics. The CCD201-20 has the smallest pixels ($13 \mu\text{m}$), followed by the CCD97 ($16 \mu\text{m}$), and the CCD60 ($24 \mu\text{m}$). The optical bench length is limited to ~ 500 mm (Figure 15);
- All of the detectors will achieve a comparable response at 850 nm (Figure 16), with a slight advantage for the devices that have the Multi-2 coating as a standard product (CCD97, CCD201-20).

Those requirements led to the choice of the 512×512 EMCCD for this system.

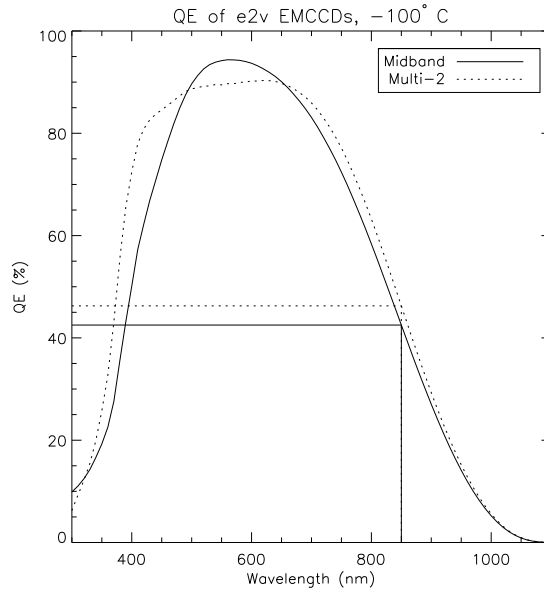


Fig 16 QE of standard Teledyne-e2v EMCCDs with respect to the coating, with an emphasis of the response at 850 nm.

6.3 The flight

The CCD97 from Teledyne-e2v was mounted in a thermoelectrically-cooled cryostat (that same as those used in the HNü cameras) and integrated with the SQ electronic controller and delivered to the Université Laval for integration. The flight is scheduled to launch in August 2018 from the Timmins airfield in northern Ontario, Canada, on the CARMEN^b platform.

7 CONCLUSION

This paper presented the characterization of a Teledyne-e2v CCD201-20 (1024×1024) with the space qualified version of Nüvü Camēras' CCD Controller for Counting Photons. The controller was built to clock EMCCDs at 10 MHz of pixel rate in a space environment and yield the imaging performance required by the WFIRST coronagraph's imagers, as well as to allow the read-out of the EMCCD through its CONV amplifier at low speed and low noise. The system was designed only with SQ components and assembled with either the SQ ICs, engineering models or exact equivalent in a commercial package. The 93 mils thick PCB made of low outgassing material was routed according to Class 3 of the IPC-2221/2222 with dual footprints to accommodate the SQ and engineering models or commercial parts. The system was integrated with a standard grade 1 CCD201-20 from Teledyne-e2v and installed in a TVAC at ABB's facilities in Quebec city. The relevant environment for achieving TRL-5 was defined according to thermal and vacuum criteria. The tests allowed to verify the compliance of the performance of the system with the Performance Evaluation Criteria derived from the performance goals for the WFIRST mission defined in [7]. During the test campaign, the system demonstrated the performance of the new low voltage and

^b<http://stratocat.com.ar/fichas-e/2017/ASP-20170409.htm>

high voltage clock designs to generate background signal levels comparable to those achieved with the commercial version of the CCCP controller, and capable of meeting the demanding applications in the future space science instrumentation such as WFIRST coronagraph.

The electronic controller was also integrated and characterized with a thermoelectrically-cooled CCD97 (512×512) from Teledyne-e2v. This system is being integrated as the coronagraph imager of the HiCiBaS stratospheric balloon mission. This mission is scheduled to take-off from Timmins, Ontario, Canada in August 2018.

Acknowledgments

The development of the space qualified EMCCD controller was made possible by funding from the Canadian Space Agency through the Science and Technology Development Program (STDP) contract N° 9F063-140572/007/MTB.

References

- 1 B. Nemati, R. Effinger, R. Demers, *et al.*, “The effect of radiation-induced traps on the WFIRST coronagraph detectors,” in *High Energy, Optical, and Infrared Detectors for Astronomy VII, Proc. SPIE* **9915**, 99150M (2016).
- 2 N. Bush, D. Hall, A. Holland, *et al.*, “Cryogenic irradiation of an EMCCD for the WFIRST coronagraph: preliminary performance analysis,” in *High Energy, Optical, and Infrared Detectors for Astronomy VII, Proceedings of SPIE* **9915**, Society of Photo-Optical Instrumentation Engineers (SPIE) (2016).
- 3 L. K. Harding, R. T. Demers, M. Hoenk, *et al.*, “Electron multiplication CCD detector technology advancement for the WFIRST-AFTA coronagraph,” in *Techniques and Instrumentation for Detection of Exoplanets VII, Proc. SPIE* **9605**, 96050F (2015).
- 4 O. Daigle, O. Djazovski, D. Laurin, *et al.*, “Characterization results of EMCCDs for extreme low-light imaging,” in *Society of Photo-Optical Instrumentation Engineers (SPIE) Conference Series, Society of Photo-Optical Instrumentation Engineers (SPIE) Conference Series* **8453** (2012).
- 5 E. T. Hamden, N. Lingner, G. Kyne, *et al.*, “Noise and dark performance for FIREBall-2 EMCCD delta-doped CCD detector,” in *UV, X-Ray, and Gamma-Ray Space Instrumentation for Astronomy XIX, Proc. SPIE* **9601**, 96010O–96010O–10 (2015).
- 6 O. Daigle, J. Turcotte, E. Artigau, *et al.*, “Preliminary characterization results of a large format 4k x 4k emccd,” in *High Energy, Optical, and Infrared Detectors for Astronomy VIII, Proc. SPIE* **10709** (2018).
- 7 D. Spergel, N. Gehrels, C. Baltay, *et al.*, “Wide-Field InfrarRed Survey Telescope-Astrophysics Focused Telescope Assets WFIRST-AFTA 2015 Report,” *ArXiv e-prints* (2015).
- 8 e2v, “CCD201-20 Back Illuminated 2-Phase IMO Series Electron Multiplying CCD Sensor,” Tech. Rep. A1A-100013 Version 4, e2v, <http://www.e2v.com/resources/account/download-datasheet/1491> (2015).
- 9 M. S. Robbins and B. J. Hadwen, “The noise performance of electron multiplying charge-coupled devices,” *IEEE Transactions on Electron Devices* **50**, 1227–1232 (2003).

- 10 O. Daigle, C. Carignan, J.-L. Gach, *et al.*, “Extreme Faint Flux Imaging with an EMCCD,” *Publications of the Astronomical Society of the Pacific* **121**, 866 (2009).
- 11 O. Côté, G. Allain, D. Brousseau, *et al.*, “A precursor mission to high contrast imaging balloon system,” in *Ground-based and Airborne Instrumentation for Astronomy VII, Proc. SPIE* **1702** (2018).
- 12 G. Allain, D. Brousseau, S. Thibault, *et al.*, “First on-sky results, performance and future of the HiCIBaS - LOWFS,” in *Adaptive Optics Systems VI, Proc. SPIE* **10703** (2018).
- 13 M. J. Wilby, C. U. Keller, F. Snik, *et al.*, “The coronagraphic Modal Wavefront Sensor: a hybrid focal-plane sensor for the high-contrast imaging of circumstellar environments,” *Astronomy and Astrophysics* **597**, A112 (2017).

© 2018 Society of PhotoOptical Instrumentation Engineers. One print or electronic copy may be made for personal use only. Systematic reproduction and distribution, duplication of any material in this paper for a fee or for commercial purposes, or modification of the content of the paper are prohibited.

© Nüvü Camēras 2018